Dominant Scattering Mechanism Identification From Quad-Pol-SAR Data Analysis

Dehbia Hanis, Karima Hadj-Rabah, *Member, IEEE*, Aichouche Belhadj-Aissa, and Luca Pallotta, *Senior Member, IEEE*

***Abstract*—Polarimetric decompositions are used to separate scatterers and identify their physical parameters by analyzing backscattering, coherence, or covariance matrices. Each cell within polarimetric synthetic aperture radar data is seen as a coherent or incoherent combination of different scattering mechanisms. However, targets are not perfectly characterized by these matrices due to the presence of noise components. The main objective of this study is to remedy the latest issue through proper noise effect elimination. Hence, we propose the reestimation of the coherence matrix, by incorporating a processing phase that searches for the number of elementary scattering mechanisms in each cell. This first step is based on the eigenvalues, which exploit the advantage of polarization basis independent of the eigenvectors. In the second step, a reduced space is defined by the eigenvectors selected, according to the cases of the first step, as those contributing to the construction of the target, excluding those judged to contribute to noise. The characteristic vector and the coherence matrix of the average target are then reconstructed in this new space in three different ways: summation of the elementary coherence matrices, applying Bernoulli's probability law, and orthogonal projection on the reduced space. Finally, the Freeman–Durden polarimetric decomposition and the H–$\overline{\alpha}$ Wishart classification are used to show the effectiveness of the process in terms of dominant scattering mechanism identification. Their application on simulated data and on fully polarized RadarSat-2 images of the city of Algiers attests to the performance of the proposed methodology to improve the identification of dominant scattering mechanisms.**

***Index Terms*—H–$\overline{\alpha}$ plane, polarimetric decomposition, polarimetric parameters, polarimetric synthetic aperture radar (PolSAR), spectral decomposition.**

I. Introduction

SYNTHETIC aperture radar (SAR) constitutes a powerful measuring tool due to its all-weather all-time imaging capability, allowing a better comprehension of our surroundings [1]. Polarimetric SAR (PolSAR) data are analyzed in order to understand the scattering mechanisms better and extract the physical characteristics and the targets' structure. The radar signal can be perceived as a coherent or incoherent addition of elementary scatterers within a resolution cell. The resulting target is then said to be coherent or incoherent and is represented by a scattering matrix for the first case and by a coherence or covariance matrix for the second [2].

Several works have been carried out with the aim of separating these scatterers and identifying the dominant scattering mechanism using polarimetric decompositions on averaged covariance or coherence matrices. The polarization bases of those matrices, obtained by employing different canonical components or eigenvectors, provide different outcomes and make the decomposition nonunique. Among the possible solutions, eigenvectors have the advantage of being base independent, making their based decomposition unique. It assumes the presence of three uncorrelated and at best statistically independent elementary targets, each represented by one of the eigenvectors and its probability of presence and contribution in the pixel by its corresponding normalized eigenvalue. This technique aims to extract uncorrelated or statically independent targets and represent the original data as a linear combination of these sources. The issue is that the elementary extracted scatterers do not always have geometrical interpretation, unlike the decomposition based on a physical model [2], [3]. The interested readers may refer to [4], [5], [6], [7], and [8] for more details.

In this context, Cloude and Pottier [9] used roll-invariant parameters based on eigenvalues and eigenvectors of the mean coherence matrix to give an interpretation of the dominant scattering mechanism. They reconstruct an average target, considered as a pure target and represented by a mean unit target vector, with the assumption that there is always a dominant *average* scattering mechanism. As a final step, the authors classify the related scattering mechanisms identified as the dominant ones using the defined H–$\overline{\alpha}$ plane. On the other side, the Huynen decomposition introduced the concept of the single target plus noise model, which is inspired by the decomposition theorem. The latter consists of a backscattered wave to a fully polarized wave corresponding to a pure target and a randomly polarized or completely depolarized wave representing a noise term [10], [11], [12]. The noise part in this case is extracted by the roll-invariant property. However, this decomposition has the disadvantage of being limited to targets presenting negatively correlated horizontal and vertical copolarized channels [3]. This assumption may not hold for all types of targets or under all conditions. An extension of this decomposition has been established by Cloude and Pottier [11], Holm and Barnes [13], and Yang et al. [14].

Manuscript received 2 April 2024; revised 18 June 2024; accepted 3 August 2024. Date of publication 7 August 2024; date of current version 26 August 2024. *(Corresponding author: Luca Pallotta.)*

Dehbia Hanis, Karima Hadj-Rabah, and Aichouche Belhadj-Aissa are with the Laboratory of Image Processing and Radiation, University of Sciences and Technology Houari Boumediene, Bab Ezzouar 16111, Algeria (e-mail: dehbia_hanis@yahoo.com; hadjrabah@hotmail.fr; houria.belhadjaissa@gmail.com).

Luca Pallotta is with the School of Engineering, University of Basilicata, 85100 Potenza, Italy (e-mail: luca.pallotta@unibas.it).

Digital Object Identifier 10.1109/JSTARS.2024.3439879

Similarly, Cloude [15] used the largest eigenvalue to identify the dominant scattering mechanism, and the results led to the ones proposed by Huynen [16]. Correspondingly, the authors in [13] and [17] raised the nonuniqueness property of the decomposition and used the three eigenvalues. Each one offers a different decomposition of the coherence matrix to an equivalent single target and a noise term. The decomposition with the first eigenvector meets Huynen's and Cloude's decompositions [10]. Then, Holm and Barnes [13] proposed a hybrid approach, combining an eigenvalue analysis, providing invariance under unitary transformations, with the concept of the single target plus noise model of the Huynen approach. The coherence matrix is decomposed into three components: a pure target that is an average target representation, a variance of the target from its average representation, and a noise term.

All the abovementioned methods do not take into consideration the number of scattering mechanisms forming the resolution cell. Therefore, the primary objective of our study is to introduce a new way of determining the mean target and noise in fully polarized SAR imagery by first identifying the number of elementary scattering mechanisms present in the resolution cell. Our operational motivation is to improve the interpretation and extraction of physical characteristics and structures from SAR data. To reach the desired outcome, the four-step process we followed can be summarized as follows.

1) Principal component analysis has been used since it gives roll-invariant and orthogonal components that represent the elementary scattering mechanisms of a more general complex target.
2) Parameters based on these eigenvalues are then calculated to distinguish the components that contribute to the pure target from the ones related to the noise contribution.
3) The characteristic vector of the mean target or its coherence matrix is reconstructed on a reduced space constructed by the eigenvectors selected in the previous step, in three ways, namely, by assuming a Bernoulli's distribution on the reduced space, by carrying out an orthogonal projection (OP), and by carrying out a summation of elementary matrices.
4) A Freeman–Durden decomposition is performed, an RGB representation is displayed, and the dominant scattering mechanism is identified using the H–$\overline{\alpha}$ plane for each reconstructed matrix.

The rest of this article is structured as follows. The basics of PolSAR concept are briefly introduced in Section II followed by a short description of the mathematical development behind the H–$\overline{\alpha}$ plane concept. Section III is devoted to the representation of our proposed method. In Section IV, the experimental results obtained by applying our method are reported, and a fruitful discussion on its performance in comparison with some state-of-the-art methods is presented as well. Finally, Section V concludes this article.

II. Background

A. Basics of PolSAR

Quad-Pol SAR systems transmit horizontally (H) and vertically (V) polarized electromagnetic waves, which can be approximated by a plane wave. Once they reach and then interact with the target, the sensor receives their echoes in both polarizations (H and V) [18]. The scattering matrix, also known as Sinclair matrix, describes the scattering properties of a target in terms of how it affects the polarization states. It is a 2×2 complex matrix whose elements depend mainly on the carrier frequency, the incident angles along with the targets' geometry, and materials. It can be expressed as [3]

$$\mathbf{S} = \begin{bmatrix} S_{HH} & S_{HV} \\ S_{VH} & S_{VV} \end{bmatrix}. \tag{1}$$

S_{TR} represents the complex scattering coefficient for the signal transmitted in T polarization and received in R polarization. The diffusion matrix can be vectorized in different ways, in order to simplify mathematical data processing and enhance its interpretation. The most common forms are lexicographic ($\mathbf{k_L}$) and Pauli-based ($\mathbf{k_p}$) representations.

When the transmitting and receiving antennas are colocated, in the case of spaceborne sensors operating in monostatic mode, the reciprocity property can be verified by stating that $S_{HV} = S_{VH}$. Thus, the scattering matrix is symmetric, and the scattering vector representations can be simplified as follows [3]:

$$\mathbf{k_L} = \begin{bmatrix} S_{HH} \\ \sqrt{2}S_{HV} \\ S_{VV} \end{bmatrix} \tag{2}$$

and

$$\mathbf{k_p} = 1/\sqrt{2} \begin{bmatrix} S_{HH} + S_{VV} \\ S_{HH} - S_{VV} \\ 2S_{HV} \end{bmatrix}. \tag{3}$$

The scattering matrix is not sufficient to analyze and identify the noncoherent targets, resulting from incoherent additions of elementary scatterers within a resolution cell [2]. Indeed, the extended targets, the targets located in a dynamic environment and subject to spatiotemporal variations, require second-order moments in coherence or covariance matrices to be described [12], [19]. Furthermore, the averaging process in spot or multilook filtering, necessary to reduce the randomness of polarimetric variables, leads to the concept of distributed target [20].

The coherence matrix $\mathbf{T}$ is built from the Pauli vector, while the covariance matrix $\mathbf{C}$ is built from the lexicographic vector according to

$$\mathbf{T} = \langle \mathbf{k_p} \mathbf{k_p}^H \rangle \tag{4}$$

$$\mathbf{C} = \langle \mathbf{k_L} \mathbf{k_L}^H \rangle \tag{5}$$

where $(\cdot)^H$ and $\langle \cdot \rangle$ represent the conjugate transpose and temporal or spatial averaging, respectively.

The coherence matrix can be written according to the covariance matrix through the following linear transformation [3]:

$$\mathbf{T} = \mathbf{E}\mathbf{C}\mathbf{E}^T. \tag{6}$$

In the monostatic case, $\mathbf{E}$ is written as follows:

$$\mathbf{E} = 1/\sqrt{2}\begin{bmatrix} 1 & 0 & 1 \\ 1 & 0 & -1 \\ 0 & \sqrt{2} & 0 \end{bmatrix}. \tag{7}$$

Under the assumption of homogeneity, the coherence matrix can be estimated by the maximum likelihood estimator, also referred to as a multilook filter, as follows:

$$\mathbf{T} = \frac{1}{n}\sum_{i=1}^{n}\mathbf{k_{P}}_{(i)}\mathbf{k_{P}}_{(i)}^{H} \tag{8}$$

where n is the number of looks and $\mathbf{k_{P}}_{(i)}$ denotes the ith one-look sample vector.

Note that, in practical applications, the coherent average of the two cross-polarized channels is used in place of the single channels [3], leading to a three-channel PolSAR image. However, this approximation can be done only if reciprocity arises [21], [22].

B. H–A–$\overline{\alpha}$ Decomposition and H–$\overline{\alpha}$ Plane

Cloude and Pottier [9] proposed a method for extracting the mean target using eigenvectors because of their basis invariant property. The coherence matrix was used to describe a noncoherent target. The aim is to be able to write this matrix as the outer product of a single target $\overline{k_0}$ with [3]

$$\mathbf{T}_3 = \sum_{i=1}^{3}\lambda_i\mathbf{v}_i\mathbf{v}_i^T = \overline{\mathbf{k_0}}\,\overline{\mathbf{k_0}}^H. \tag{9}$$

The ith eigenvector of the averaged coherence $\mathbf{T}_3$ matrix has been parameterized for a medium without azimuthal symmetry as follows:

$$\mathbf{v}_i = \exp(j\phi_i)\begin{bmatrix} \cos(\alpha_i) \\ \sin(\alpha_i)\cos(\beta_i)\exp(j\delta_i) \\ \sin(\alpha_i)\sin(\beta_i)\exp(j\gamma_i) \end{bmatrix}. \tag{10}$$

Considering a statistical model as a three-symbol Bernoulli process, the characteristic vector of the mean target, $\mathbf{v_0}$, is described by the unit vector of the same form as (10), with the mean values of the various parameters defined as

$$\overline{\alpha} = \sum_{i=1}^{3}p_i\alpha_i;\ \overline{\beta} = \sum_{i=1}^{3}p_i\beta_i;\ \overline{\gamma} = \sum_{i=1}^{3}p_i\gamma_i;\ \overline{\delta} = \sum_{i=1}^{3}p_i\delta_i$$
$$\text{with}\quad p_i = \frac{\lambda_i}{\sum_{i=1}^{3}\lambda_i}. \tag{11}$$

The mean target is then defined by

$$\overline{\mathbf{k_0}} = \sqrt{\overline{\lambda}}\mathbf{v_0}\quad\text{with}\quad \overline{\lambda} = \sum_{i=1}^{3}p_i\lambda_i. \tag{12}$$

Once a model of the average target had been defined, an H–$\overline{\alpha}$ plane was introduced to identify the dominant scattering mechanism (see Fig. 1). In fact, three roll-invariant parameters, i.e., entropy, anisotropy, and mean alpha angle, were used. The entropy

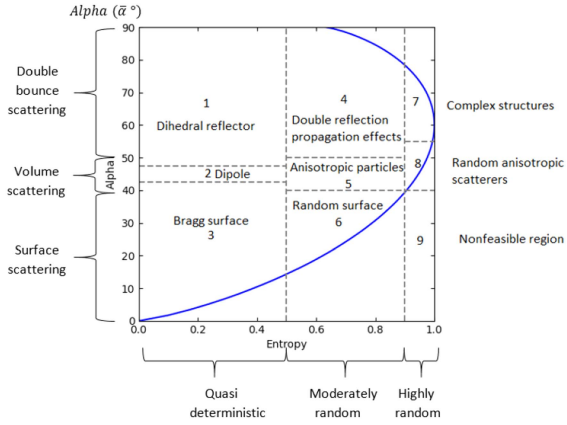

Fig. 1. H–$\overline{\alpha}$ plane [3].

H measures the randomness of the scattering [7] and describes the purity of the scattering [23]. $H = 1$ ($\lambda_1 = \lambda_2 = \lambda_3 = 1/3$) corresponds to a random scattering mechanism, and $H = 0$ (single eigenvalue case) corresponds to a unique scattering mechanism, while the alpha angle ($0° \leq \alpha \leq 90°$) constitutes the main parameter for identifying the type of the dominant scattering mechanism [3], [23]. Moreover, $\alpha \approx 0°$ denotes dominant Bragg scattering (odd bounce scattering), while $\alpha \approx \pi/4$ indicates the presence of dipole structure (dominant volume scattering) and $\alpha \approx \pi/2$ indicates the presence of dihedral structures (dominant double bounce scattering).

To overcome the misclassification occurring due to the same H for different eigenvalues, the anisotropy A parameter has been introduced. Their respective formulas are

$$H = \sum_{i=1}^{3} -p_i\log_3(p_i)\quad\text{and}\quad A = \frac{\lambda_2 - \lambda_3}{\lambda_2 + \lambda_3}. \tag{13}$$

Comprised between 0 and 1, A measures the relative importance of the second and third eigenvalues of the coherence matrix [3], [7]. This parameter can be employed as a source of discrimination only when $H > 0.7$. This is due to the fact that for lower entropies, the SAR system noise highly affects the values of the second and third eigenvalues [19].

Furthermore, different descriptors corresponding to the different combinations between H and A images have been proposed to distinguish between different types of scattering processes. The single scattering mechanism is represented by $P_1 = (1-H)(1-A)$, the random scatterers by $P_2 = H(1-A)$, the scatterers with two scattering mechanisms with one dominant and a second with medium probability by $P_3 = (1-H)A$, and the scatterers with two scattering mechanisms with same probabilities by $P_4 = HA$ [24].

In [25] and [26], the classification of dominant scattering mechanisms in PolSAR images is formulated as a multiple-hypothesis test solved through the use of model-order selection rules. Moreover, Biondi et al. [27] classified dominant polarizations in PolSAR images, extending the dominant eigenvalue classification scheme proposed in [25] by integrating reduced-size classifiers based on model-order selection rules [28].

III. Proposed Method

The multidimensional covariance matrix is considered the best descriptor in the data science framework. Similarly, in PolSAR, it constitutes a power-domain representation of the scattering properties. Its estimation, however, can be challenging, particularly in the case of heterogeneous areas, where a variety of scatterers having distinct material properties, elevations, and orientations are present. Two different strategies can be performed to estimate the covariance matrix: the local and nonlocal approaches [29]. While the former exploits the information contained only on the neighbors located close to the pixel of interest, the latter exploits the information available on all the pixels with a certain degree of similarity.

From a mathematical perspective, the Pauli vector, whose components represent the surface, dihedral and volume backscattering, is used to process the coherence matrix. The use of the coherence matrix instead of the covariance matrix helps to better distinguish the three basic elementary scattering mechanisms, knowing that its diagonal elements represent their power and that the off-diagonal elements represent their covariances.

The coherence and covariance are both positive-semidefinite Hermitian matrices (namely, $\mathbf{C}_{ji}^{*} = \mathbf{C}_{ji}$ and $\mathbf{T}_{ij} = \mathbf{T}_{ji}^{*}$), and their real nonnegative eigenvalues are the same, but their eigenvectors are different. The coherence matrix expression formula is given by

$$\mathbf{T} = \sum_{i=1}^{3} \lambda_i \mathbf{v}_i \mathbf{v}_i^H = \mathbf{V}\mathbf{\Lambda}\mathbf{V}^H \tag{14}$$

where $\mathbf{V}$ and $\mathbf{\Lambda}$ account for the eigenvectors' matrix whose column vectors are orthogonal to each other (i.e., $\mathbf{v}_i^H \mathbf{v}_j = 0$ when $i \neq j$) and the eigenvalues' matrix whose diagonal elements are the corresponding eigenvalues λ_i in ascending order $(\lambda_1 \geq \lambda_2 \geq \lambda_3 \geq 0)$, respectively.

By taking advantage of the spectral decomposition uniqueness, we propose to calculate two metrics based on the eigenvalues of the coherence matrix known by its mathematical orthogonality. In fact, their behavior can be analyzed in an attempt to control the pertinent properties to be preserved. Then, a cutoff threshold T_h relative to the purity of the pixels is applied in order to distinguish and identify the case scenarios: single scattering mechanisms, scatterers having mixed mechanisms, and random scatterers. The determination of the threshold is related to the cumulative percentage of variance to be outpaced. Depending on the data's particularity and the application's requirements, practical cutoff levels are mainly in the range of 70–95% of the total variation cumulative percentage [30]. The proposed metrics can be formulated as follows:

$$\text{metric}_k = \frac{\sum_{i=1}^{k} \lambda_i}{\lambda_1 + \lambda_2 + \lambda_3}. \tag{15}$$

Note that k can be equal to 1 or 2, and that $\text{metric}_k > T_h$ should be satisfied.

The role of T_h consists of determining the suitable amount of valuable information without serious loss. According to the literature, only subjective methods are disposable, and no evaluation technique exists [31]. In these circumstances, a testing procedure was established, and the most appropriate value was selected. It corresponds to the mean ratio of the pixels where the average value of the three eigenvalues was greater than 75% of its average over the whole image. In our study, this value was found to be 0.92. In the following, scattering events' identification can be carried out as follows.

1) If the number of retained components is equal to 1 $(k = 1)$, it means that the target–wave interaction within the resolution cell shows the same behavior ⇒ single scattering mechanism.
2) In case the maintained elements are 2 $(k = 2)$, the objects within the pixel of interest are exhibiting two distinct behaviors ⇒ mixed scattering mechanism.
3) The remaining case scenario involves targets with arbitrary behaviors ⇒ random scattering mechanism.

Once the identification phase has been completed, the next step is to reconstruct the mean target vector or coherence matrix from the selected k components. To this end, we have proposed three distinct ways: elementary summation (ES), modified Bernoulli (MB), and OP. The first one consists of reconstructing the average coherence matrix by summing the elementary matrices as follows:

$$\tilde{\mathbf{T}}_{\text{ES}} = \sum_{i=1}^{k} \lambda_i \mathbf{v}_i \mathbf{v}_i^H. \tag{16}$$

The second way consists of considering a statistical model similar to the Bernoulli process with the identified number of scattering mechanisms k instead. The characteristic vector of the mean target $\overline{\mathbf{k}}_{\text{MB}}$ is then described by

$$\overline{\mathbf{k}}_{\text{MB}} = \sqrt{\overline{\lambda}}\mathbf{v}_{\text{MB}} \quad \text{with} \quad \overline{\lambda} = \sum_{i=1}^{k} p_i \lambda_i. \tag{17}$$

Notice that $\mathbf{v}_{\text{MB}}$ is a unit vector of the same form as that in (10), with average values of the different parameters of (11) with a difference in the number of summed components, namely k instead of 3. The calculation of the mean values becomes in this case

$$\overline{\alpha} = \sum_{i=1}^{k} p_i \alpha_i, \overline{\beta} = \sum_{i=1}^{k} p_i \beta_i, \overline{\gamma} = \sum_{i=1}^{k} p_i \gamma_i, \overline{\delta} = \sum_{i=1}^{k} p_i \delta_i$$
$$\text{with} \quad p_i = \frac{\lambda_i}{\sum_{i=1}^{k} \lambda_i}. \tag{18}$$

This mean vector is then used to reconstruct the coherence matrix.

$$\tilde{\mathbf{T}}_{\text{MB}} = \overline{\mathbf{k}}_{\text{MB}} \overline{\mathbf{k}}_{\text{MB}}^H \tag{19}$$

The third way consists of reconstructing another characteristic vector by OP of the Pauli vector on the reduced plane constructed by the retained eigenvectors. The OP of the vector $\mathbf{k_p}$ onto an orthonormal basis $\mathbf{U} = [\mathbf{v_1}, \ldots, \mathbf{v_k}]$, where each $\mathbf{v}_i, i = 1, \ldots, k$, is a base vector given by the formula:

$$\text{proj}_{\mathbf{U}}(\mathbf{k_p}) = \mathbf{U}(\mathbf{U}^H\mathbf{U})^{-1}\mathbf{U}^H\mathbf{k_p}. \tag{20}$$

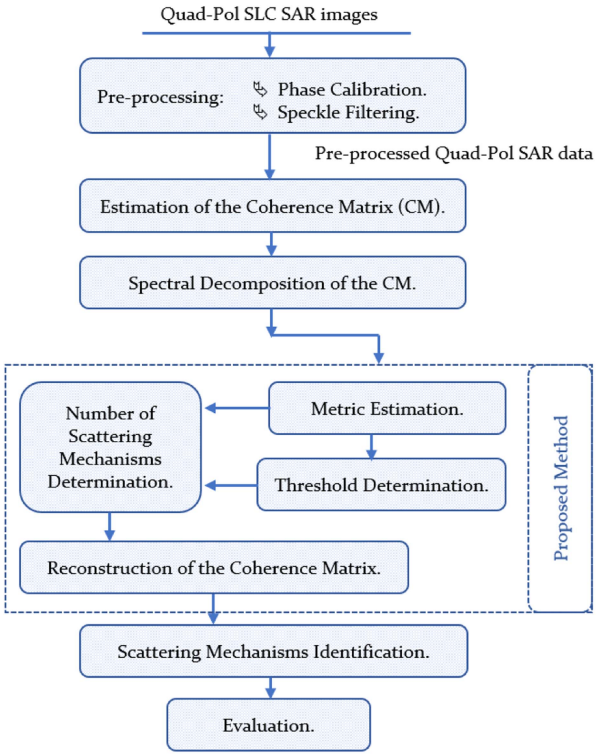

Fig. 2. Block diagram of the proposed method.

If projected onto the eigenvector basis of the coherence matrix, which is a Hermitian matrix, the eigenvectors are orthogonal and thus satisfy the following condition:

$$\mathbf{U}^{-1} = \mathbf{U}^{H}. \tag{21}$$

The projection is then written as

$$\overline{\mathbf{k}}_{\mathrm{OP}} = \mathrm{proj}_{\mathbf{U}}(\mathbf{k_p}) = \mathbf{U}\mathbf{U}^{H}\mathbf{k_p} \tag{22}$$

and

$$\tilde{\mathbf{T}}_{\mathrm{OP}} = \overline{\mathbf{k}}_{\mathrm{OP}}\overline{\mathbf{k}}_{\mathrm{OP}}^{H}. \tag{23}$$

This OP preserves distances and angles. On the reduced space, $\mathbf{U}$ is a $3 \times k$ matrix, so $\mathbf{U}\mathbf{U}^{H}$ is a 3×3 one.

To sum up, the fundamental steps followed during our proposed processing are summarized in the flowchart of Fig. 2. In fact, after a calibration of the polarimetric data and speckle filtering phase, we procured a local spectral decomposition of the coherence matrix, in order to calculate the proposed metrics from the trace of the eigenvalues' matrix, as described above. After an adequate identification, we reconstruct the coherence matrix according to three distinct ways (ES, MB, and OP) in an effort to identify the number of elementary scattering mechanisms present in a single cell relative to the purity threshold established. The validation by Freeman–Durden decomposition and H–$\overline{\alpha}$ space constitutes the final step. The latter can be achieved by a Wishart classification, where each single pixel is assigned to the class whose center minimizes the Wishart distance calculated between the reconstructed coherence matrix $\tilde{\mathbf{T}}$ and the latest class center $\mathbf{T}_i$, $i = 1, \ldots, 8$. Note that, for the eight possible classes, $\mathbf{T}_i$ is computed using the subsequent formula

$$\mathbf{T}_i = \sum_{j=1}^{N_i} \hat{\mathbf{T}}_{\mathrm{SCM}}(j) \tag{24}$$

where N_i and $\hat{\mathbf{T}}_{\mathrm{SCM}}(j)$ account for the number of pixels assigned to the class i and the coherence matrix of the jth resolution cell on the class in question, respectively.

IV. Results and Discussion

In this section, the performance of the proposed strategies for dominant scattering mechanism identification is assessed. In particular, to evaluate the effectiveness of various techniques, both simulated and real PolSAR data are considered.

A. Simulated Data

To quantitatively evaluate the effectiveness of the proposed framework, a simulating scenario is herein considered. It consists in generating the coherence matrix of mixed scattering mechanisms, by combining different contributions a_s, a_v, and a_{db} representing the Bragg surface, oriented dipole, and dihedral scatterings. They are expected to be classified, respectively, as class 3, class 2, and class 1 in the H–$\overline{\alpha}$ plane, and represented by the Yamaguchi models in [7] as $\mathbf{T}_s$, $\mathbf{T}_v$, and $\mathbf{T}_{db}$, ensuring a dominant mechanism, as follows:

$$\mathbf{T} = a_s\mathbf{T}_s + a_{db}\mathbf{T}_{db} + a_v\mathbf{T}_v. \tag{25}$$

In the following, each of the three methods is applied for the reestimation of the coherence matrix, and the dominant scattering mechanism detection procedure is used to reveal them. More precisely, the canonical scattering mechanisms (comprising dihedral, oriented dipole, and Bragg surface) are generated according to [7]

$$\mathbf{T}_s = \begin{bmatrix} 1 & \beta & 0 \\ \beta & |\beta|^2 & 0 \\ 0 & 0 & 0 \end{bmatrix}, \quad \mathbf{T}_{db} = \begin{bmatrix} |\alpha|^2 & \alpha & 0 \\ \alpha^* & 1 & 0 \\ 0 & 0 & 0 \end{bmatrix}$$
$$\mathbf{T}_v = 1/4 \begin{bmatrix} 2 & 1 & 1 \\ 1 & 0.5 & 1 \\ 2 & 1 & 2 \end{bmatrix} \tag{26}$$

with $|\alpha| < 1$ and $|\beta| < 1$ (in our simulations, we set α and β equal to 0.2). In the subsequent analysis, the Bragg surface scattering is set as the dominant one, with different percentages that vary from 50% to 80% (precisely, 10^3 values for the dominant scattering mechanism are used). For each parameter setting, simulations are repeated following the classic Monte Carlo approach, performing 10^5 independent trials. The coherence matrix is hence generated at each trial sharing the above-described mixed scattering mechanisms, randomly combining the other two nondominant mechanisms.

Table I reports the number of times (expressed in percentages) the dominant mechanism is correctly classified, when the dominant Bragg surface is equal to 50%, 60%, 70%, and 80%. The displayed results show the outcome of each variant of the

TABLE I
PERCENTAGE OF DETECTED DOMINANT BRAGG SURFACE SCATTERING MECHANISM

	50%	60%	70%	80%
$\mathbf{T}$	11.3%	16.6%	35.9%	100%
$\mathbf{T}_{\mathrm{ES}}$	67.9%	86.5%	100%	100%
$\mathbf{T}_{\mathrm{OP}}$	67.2%	85.3%	97.6%	100%
$\mathbf{T}_{\mathrm{MB}}$	93.1%	100%	100%	100%

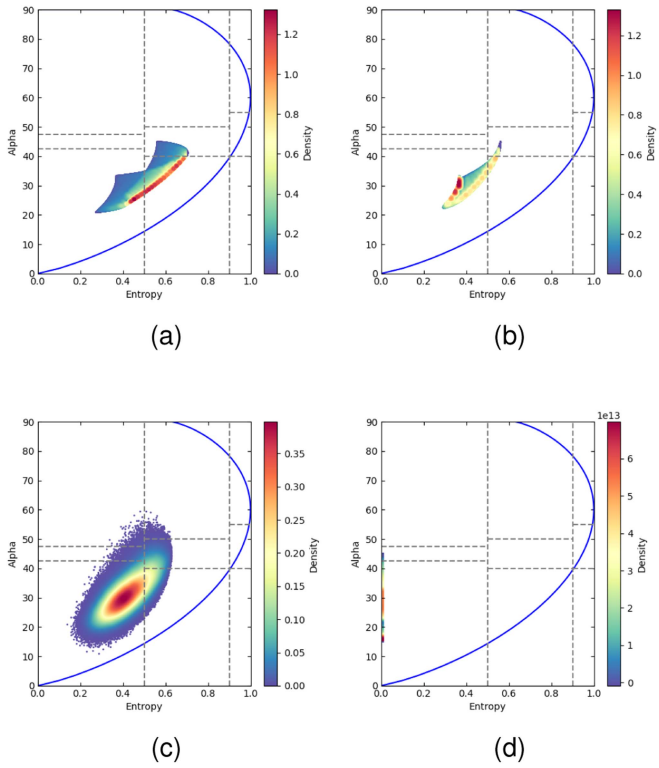

Fig. 3. H–$\overline{\alpha}$ plane. (a) $\mathbf{T}$. (b) $\mathbf{T}_{\mathrm{ES}}$. (c) $\mathbf{T}_{\mathrm{OP}}$. (d) $\mathbf{T}_{\mathrm{MB}}$.

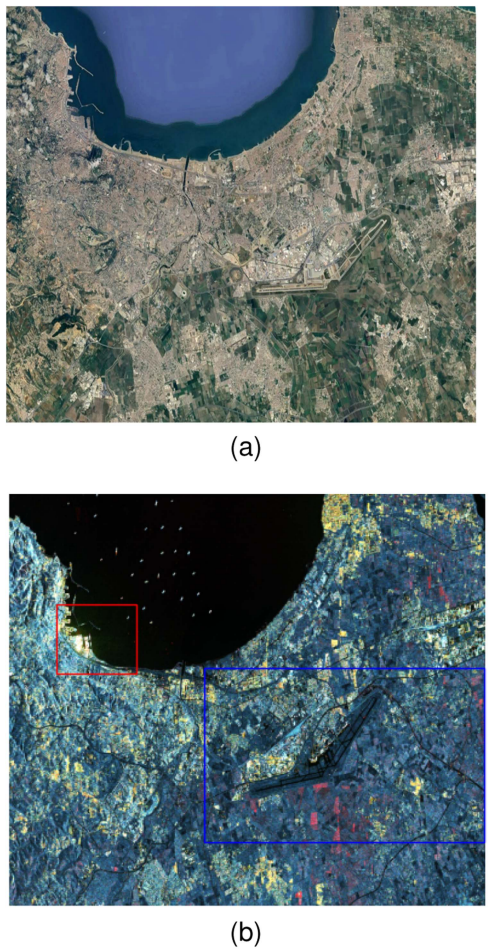

Fig. 4. (a) Optical image of the scene from Google Earth. (b) RGB coherence matrix's eigenvalues (blue and red boxes limit the areas of interest).

proposed framework with respect to the classic counterpart. By inspection, it is evident that the proposed scheme overcomes the competitor, with the MB reaching the best detection performance. In addition, it is not surprising that increasing the percentage of the dominant mechanism produces a consequent increase in the performance of each analyzed method.

For a detailed visualization of the findings, the overall H–$\overline{\alpha}$ plane for the simulated environment is plotted in Fig. 3. In the overall study, the dominant Bragg scattering mechanisms were extracted and identified by the ES, OP, and MB methods at the percentages of 85.15%, 84.68%, and 98.43%, respectively. Differently, the classic mixed scattering coherence matrix only reaches 35.35%. It is worth underlining that for the ES and OP algorithms, the dominant mechanism in the misclassified data has been interpreted mainly as class 6. This can be explained by observing that it is essentially a random surface, which can be seen as a mixture of surface and double bounce effects. As a matter of fact, the rougher the surface, the higher the entropy. The graphs show that, even though the OP map spans six classes, the percentage of values within classes 1, 2, and 4 is less than 1%, rendering it negligible.

B. Real Data

Our study was carried out on data acquired over an Algerian area, covering lands that have distinct surface characteristics and maintain numerous types of use. For visual comparison purposes, we displayed in Fig. 4(a) an optical image of the scene obtained from Google Earth. At first hand, it shows that part of the Mediterranean Sea, seaside, international airport, urban zones, and agricultural fields are covered. Ultimately, the PolSAR data used consist of a fully polarized RadarSat-2 image whose coherence matrix's eigenvalues are displayed in the RGB image of Fig. 4(b). The blue and red boxes limit the areas of interest selected for further analysis and evaluation. The sensor parameters are reported in Table II.

To study the improvement that our proposed method ensures, we laid out the intermediate attainments before the final outcome. For that, results of both metrics and number of scattering mechanisms will be displayed for the entire scene. However, the polarimetric decomposition and Wishart H–$\overline{\alpha}$ classification algorithm will be applied on the delimited zones [see Fig. 4(b)],

TABLE II
RADARSAT-2 PARAMETERS

Parameter	Quantity
Wavelength	5.5 [cm]
Sensor Altitude	798 [km]
Incidence Angle	38.34 to 39.81 [degrees]
Nominal Resolution [Rng × Az]	5.2 × 7.6 [m]
Range Resolution	4.74 [m]
Look Direction	Right
Pass	Descending
Acquisition mode	Fine Quad Polarization

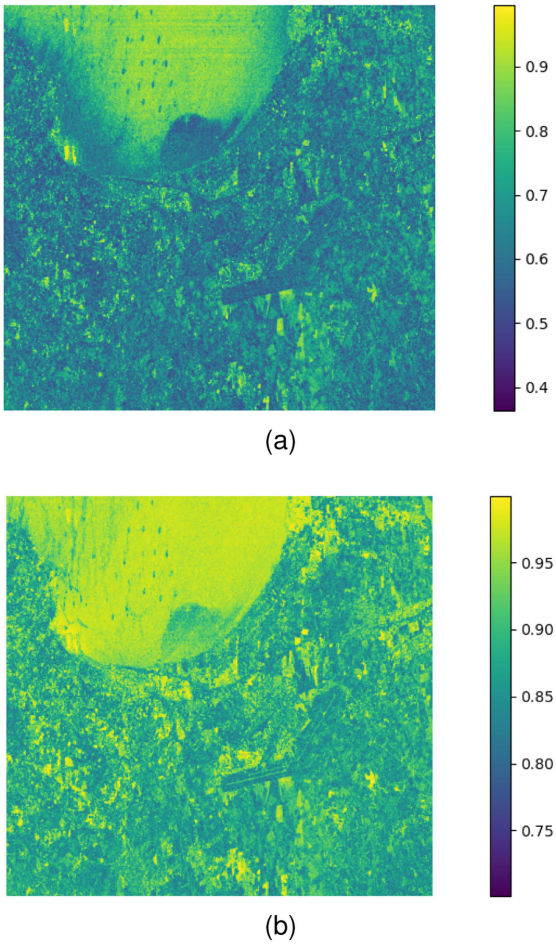

Fig. 5. Proposed (a) metric$_1$ and (b) metric$_2$ of the scene.

for a better display and result analysis. The first area [see the blue box in Fig. 4(b)] covers the airport, the main freeway, as well as some sown and unsown farmland. The second one contains mainly the port, the sea, and urban structures [see the red box in Fig. 4(b)].

The first work portion consists of metrics' estimation, as designated in the block diagram of Fig. 2. The metrics were calculated for each resolution cell according to (15), and their values are displayed in Fig. 5. The first metric$_1$ measures the importance of the first eigenvalue compared to the two others, while the second metric$_2$ expresses the ratio of the first and second eigenvalues.

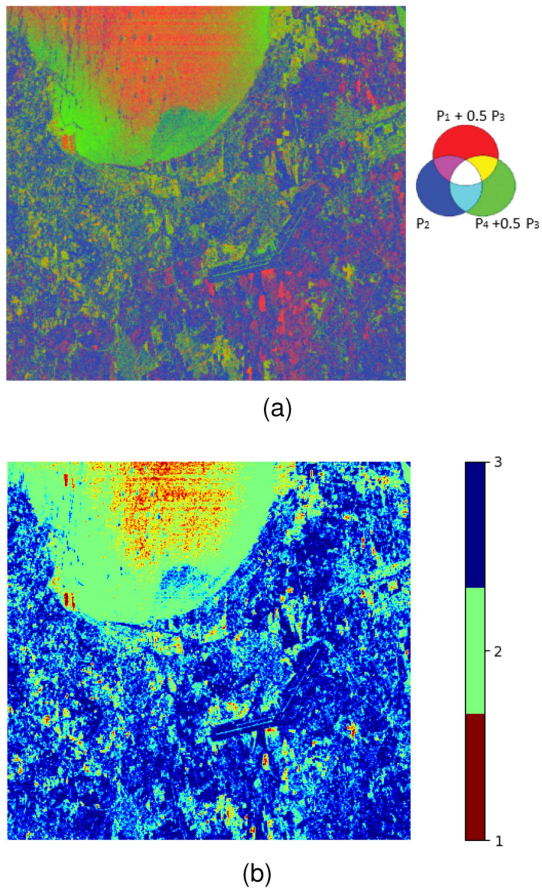

Fig. 6. Number of scattering mechanisms determined by (a) the method proposed in [3] with four-band RGB representation inspired by Yamaguchi [7] and (b) the proposed method.

The second portion covers the threshold determination. Once this step is performed, the number of scattering mechanisms can be estimated. Fig. 6(b) shows the obtained results. As shown by its color bar, there are three possibilities. The red and green colors account for single and double dominant mechanisms, while the blue represents random scattering cases. To have a better vision, we generated in Fig. 6(a) an RGB image of the classic method proposed by Lee and Pottier [3]. Note that this four-band RGB representation is inspired by Yamaguchi characterization [7] (as illustrated by its color map on the right-hand side). Actually, red and blue appear for one dominant and random scattering correspondingly, although yellow and green depict the case of two mechanisms with and without one dominant, respectively. It can be seen from visual comparison that the proposed method has an easier identification compared to the state of the art. In general, it can be perceived from Fig. 6 that a few resolution cells have only one dominant scatterer since most of them possess more than one.

The third part of our proposed method concerns the rees-timation of the coherence matrix according to the number of scattering mechanisms determined. In this phase, three ways have been used to achieve the task ES, MB, and OP, as explained in Section III. Then, we performed polarimetric decomposition.

In Figs. 7 and 8, we displayed the RGB composite from the Freeman–Durden decomposition, over the first and second zoomed-in areas, of the original data and the reconstructed data in the previous phase. It can be seen that the three variants of the proposed method provide well-distinguished resolution cells, a better contrast, and a variety of colors.

In fact, the reconstructed vectors obtained by ES, MB, and OP [see Fig. 7(b)–(d)] show more pixels colored in blue in recently sown agricultural land and bare land represented by Bragg surfaces. They also manifest pixels in green in forested areas. The results of the second variant (ES) show the brightest colors, a purer blue on bare soil, a more intense pinkish-red on built-up areas, and a lighter green on areas with dense trees.

In the second area displayed in Fig. 8, the Freeman–Durden decomposition findings show that metal containers appear yellow with the original dataset. The latter is a result of a red and green composition, representing double bounce and volume scattering. With the proposed method, these objects become redder, which means that a double bounce mechanism is highlighted, while the volumetric one is more or less filtered from one reestimation way to another. The ES variant is the one that has extracted the most double bounce. In addition, built-up areas are best highlighted by it, since they appear in magenta (a mixture of red and blue). This illustrates the presence of two scattering mechanisms: the double bounce of built-up areas and the surfaces between built-up areas.

The last part of this process focuses on identifying the scattering mechanisms using the H–$\overline{\alpha}$ Wishart classifier. The obtained results are displayed in Figs. 9 and 10. It can be observed in both the cases that several pixels originally categorized as class 6 [see Figs. 9(a) and 10(a)] are classified as class 3 with the reconstructed datasets according to the proposed method [see Figs. 9(b)–(d) and 10(b)–(d)]. Indeed, zooming in on unseeded or recently seeded farmland, identified by a polygon in Fig. 7, we found out that 12%, 14%, and 36% more in the area were identified as Bragg surface with ES, OP, and MB, respectively, instead of a rough surface with random behavior by the classical method. A similar discrepancy occurred with pixels initially assigned to classes 7 and 8 converted to classes 4 and 5, respectively. To elucidate and analyze these noticeable variations, we investigate the underlying causes contributing to the alteration in classification outcomes through the H–$\overline{\alpha}$ plane reported in Fig. 1.

To dig deeper into details, Fig. 11 reports the H–$\overline{\alpha}$ Wishart classification of the urban area delineated with a labeled polygon in Fig. 9. From a first visual inspection, it is evident that the MB method provides a clusterization of the pixels' area into only three classes (viz., classes 1–3), whereas the others essentially distribute the pixels to the first six classes. Moreover, the class histogram of the four variants with reference to the H–$\overline{\alpha}$ classification of Fig. 11 is depicted in Fig. 12. All three methods reported more pixels in the low-entropy classes 1–3 and fewer in the other high-entropy classes compared to the classic version.

As before, Fig. 13 shows the class histogram of the four classifiers with reference to the H–$\overline{\alpha}$ Wishart classification of the whole second zoomed-in area [see the red box in Fig. 4(b)]. The figure shows that the three proposed variants estimated

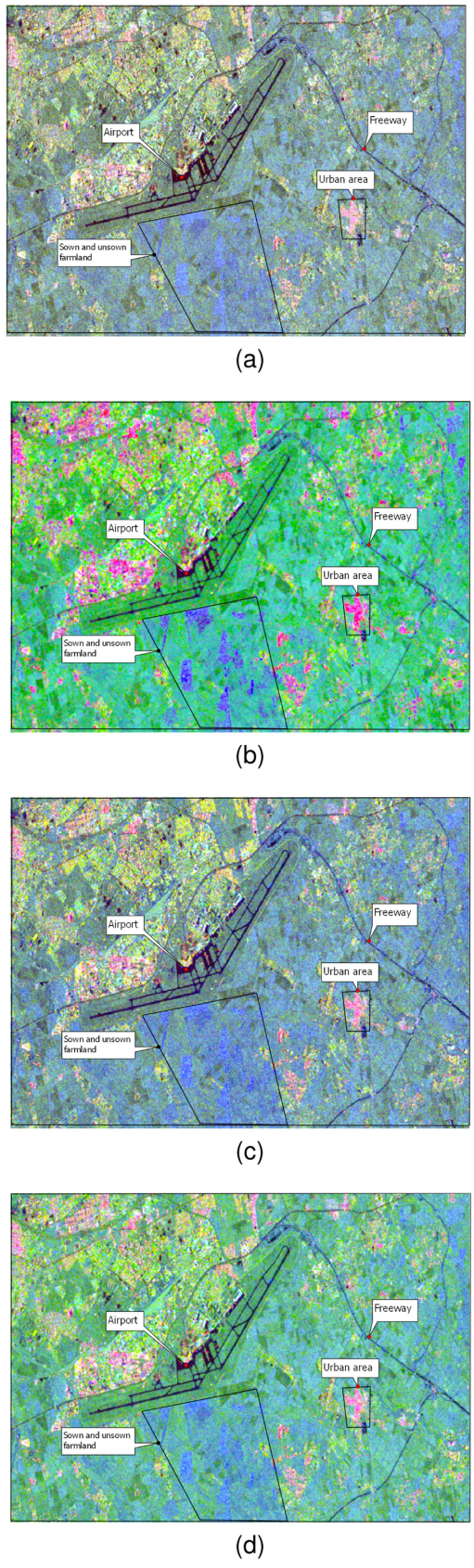

Fig. 7. Freeman–Durden decomposition applied to the first zoomed-in area [blue box in Fig. 4(b)] using (a) the original dataset, and the reconstructed dataset by the proposed method according to (b) ES, (c) MB, and (d) OP.

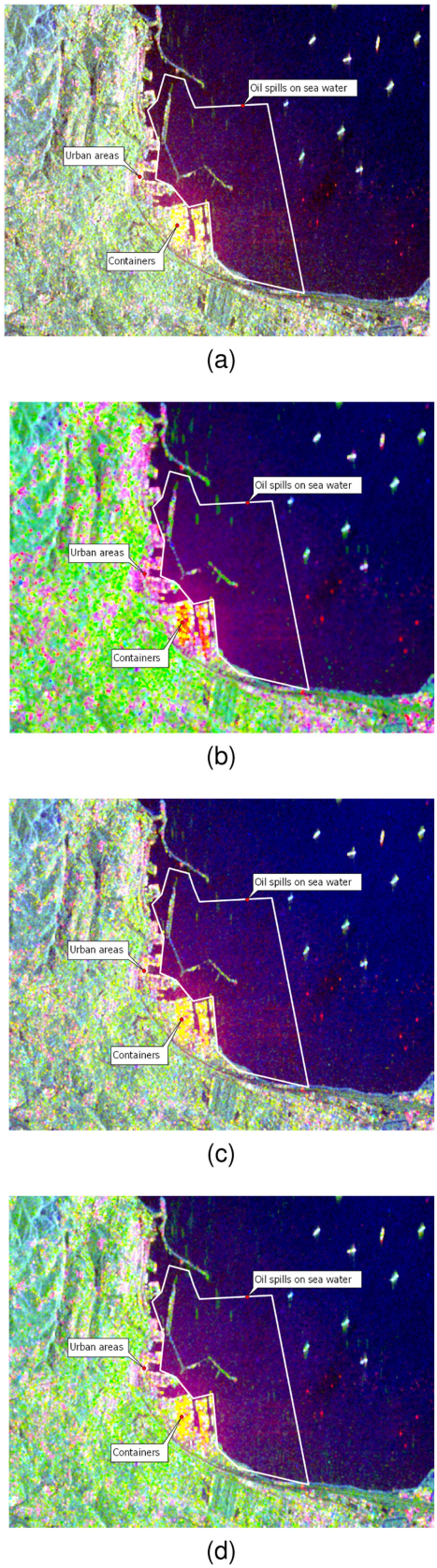

Fig. 8. Freeman–Durden decomposition applied to the second zoomed-in [red box in Fig. 4(b)] area using (a) the original dataset, and the reconstructed dataset by the proposed method according to (b) ES, (c) MB, and (d) OP.

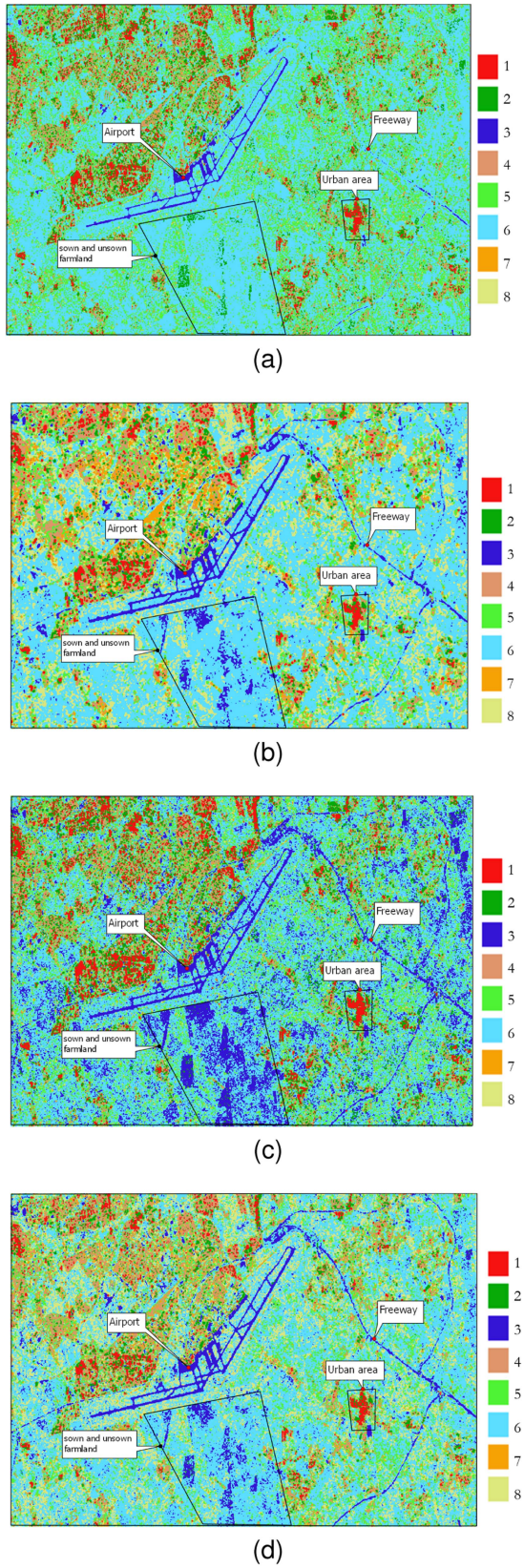

Fig. 9. H–$\overline{\alpha}$ Wishart classification applied to the first zoomed-in area [blue box in Fig. 4(b)] using (a) the original dataset, and the reconstructed dataset by the proposed method according to (b) ES, (c) MB, and (d) OP.

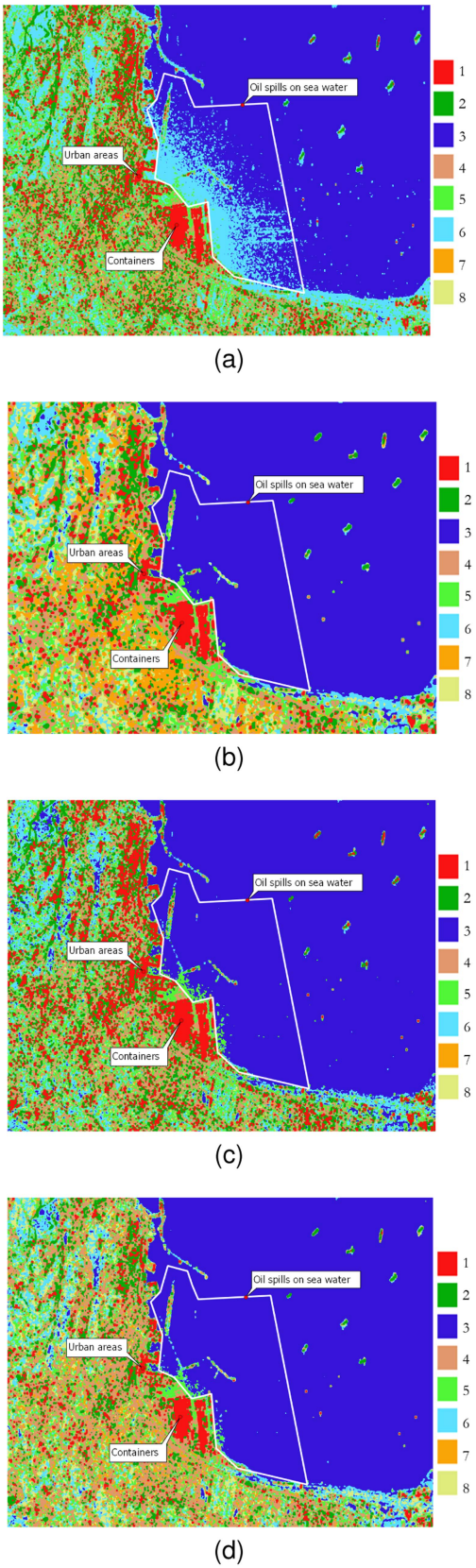

Fig. 10. H–$\overline{\alpha}$ Wishart classification applied to the second zoomed-in area [red box in Fig. 4(b)] using (a) the original dataset, and the reconstructed dataset by the proposed method according to (b) ES, (c) MB, and (d) OP.

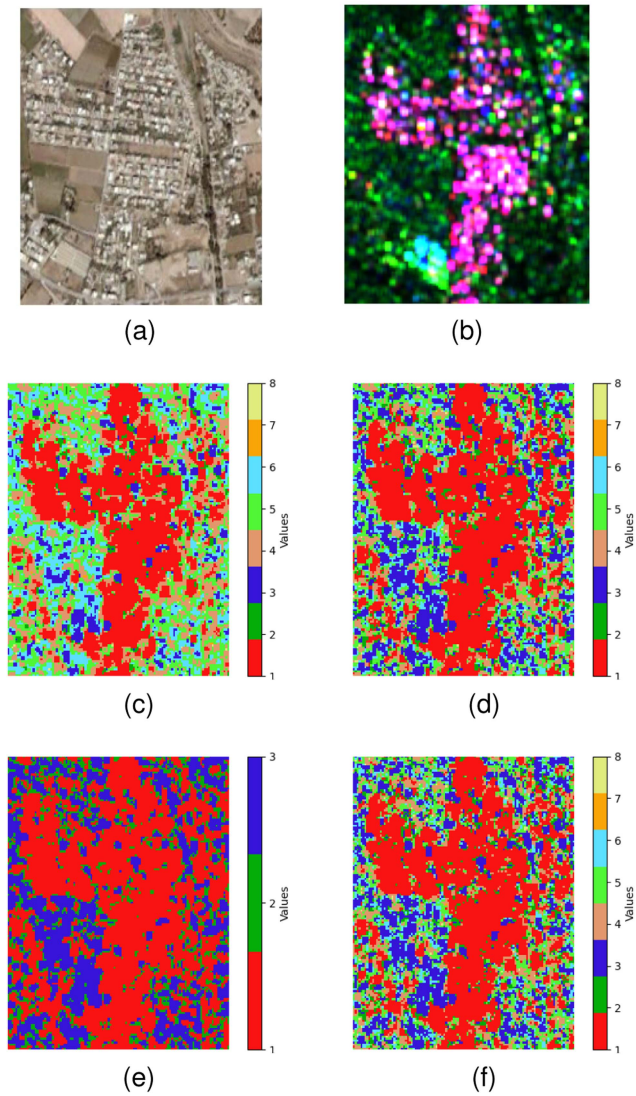

Fig. 11. (a) Google Earth optical image and (b) RGB SAR composite of the urban area denoted by a polygon in Fig. 9. H–$\overline{\alpha}$ Wishart classification generated using the coherence matrix: (c) $\mathbf{T}$, (d) $\mathbf{T}_{\mathrm{ES}}$, (e) $\mathbf{T}_{\mathrm{MB}}$, and (f) $\mathbf{T}_{\mathrm{OP}}$.

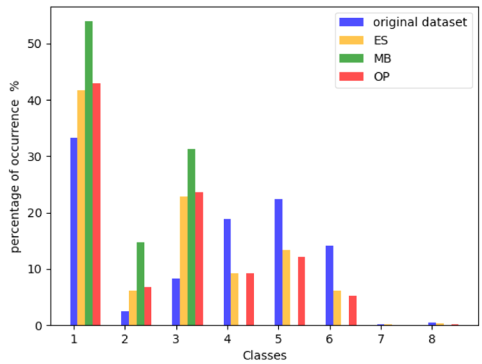

Fig. 12. Class histogram of the four classifiers applied to the urban area delimited by a polygon in Fig. 11.

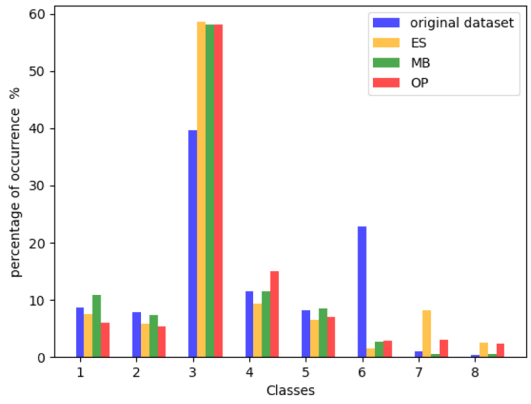

Fig. 13. Class histogram of the four classifiers with reference to the H–$\overline{\alpha}$ Wishart classification of the second zoomed-in area of Fig. 10.

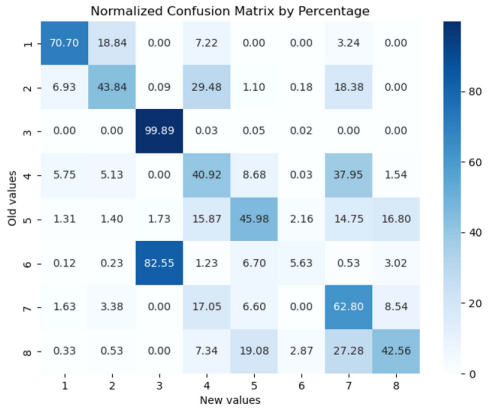

(a)

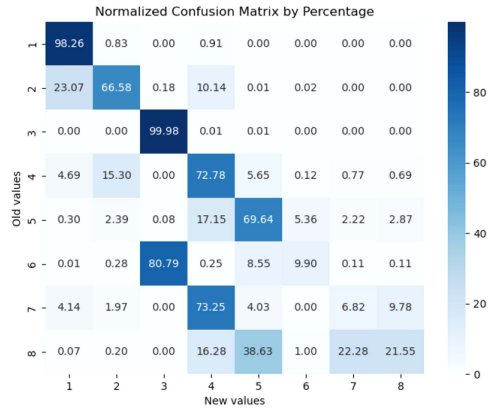

(b)

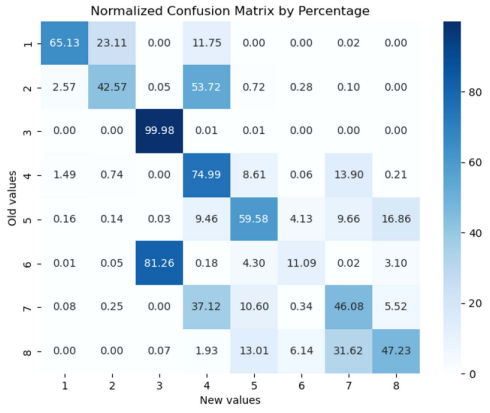

(c)

Fig. 14. Confusion matrix between the original method and the proposed method according to (a) ES, (b) MB, and (c) OP approaches.

almost the same area in the surface scattering mechanism. In fact, areas originally classified as random scattering mechanisms (class 6), delineated by a polygon in Fig. 10(a)–(d), are being reclassified as surface scattering (class 3) once the proposed method is applied. This is due to the effect of the polluting oil from ships in the seawater at the port, which led to a random attitude classified as class 6 using the original data. Thanks to the proposed approach, the randomness has been eliminated, bringing out the real dominant scattering mechanism.

The behavior can be explained by the fact that the entropy of the newly estimated matrices according to our proposed variants is lower than that of the original data. The latter is the consequence of reducing the scattering randomness in each resolution cell after the extraction of the dominant scattering mechanism and the elimination of the secondary ones.

To further investigate this effect, we plotted in Fig. 14 the confusion matrix between the result of the classification of the original data, taken as a reference, and each of the three classification results of the matrices generated by the proposed variants. It can be perceived that in urban zones, the initial categorization yields to class 4 since the entropy is medium with multiple scattering suggesting dense filling of localized scattering centers. However, after reestimation of the coherence matrix, the entropy value decreased and the scattering turned into a double bounce, which corresponds without fault to class 1. Similarly, in isolated vegetated sectors, early grouping suggests class 5 seeing that medium entropy and vegetation scattering are the showcase. Nevertheless, the proposed method application improved the entropy while maintaining the same scattering. The latter become close to class 2, which describes better needle-like aspect of those targets. Finally, agricultural land with light vegetation or bare soil is better delimited after this reestimation. Initially classified pixels in class 6 have been reclassified as Bragg surface in class 3. It can be noted that some isolated trees, which should be classified as class 2 according to the H–$\overline{\alpha}$ plane, have been lost.

The extraction of the dominant mechanism eliminated the effect of propagation of roughness and highlighted the surface aspect of the region. The reason for that deviation between the classifiers is that the dominant scattering mechanism can be confused and masked by the others in the traditional method. The rectification carried out with our proposed method acknowledges the positive impact that thresholding ahead of reconstructing the coherence matrix can have over identifying the dominant scattering mechanisms.

We can conclude that the coherence matrix reestimation method generalizes the details, so the contrast appears better, and the colors are more intense. The buildings are pinker (shade of red), the surface scattering areas are darker blue, and the volume scattering pixels are greener. However, this method may result in the loss of details, such as a few isolated trees on bare land.

V. Conclusion

The identification of the number of scattering mechanisms is a delicate task in PolSAR data analysis due to the nonuniqueness of the available developed state-of-the-art polarimetric decompositions. In this article, we propose to estimate the dominant scattering mechanisms based on the spectral decomposition of the coherence matrix. With the assumption of dominant mechanism presence, the proposed method decomposes the matrix into orthogonal uncorrelated subelements. It is then reconstructed by projection onto the elements deemed to make up the mean target, and the remainder is considered as noise. Three distinct ways have been considered: ES, MB, and OP. An H–$\overline{\alpha}$ Wishart classification is then applied to give physical meaning to the dominant scattering mechanisms. Unlike the classical method, where the process is considered as Bernoulli for the estimation of the mean target, and the three eigenvalues and eigenvectors are taken in the model of the mean target, our proposed method decides first which values contribute to the target composition and which ones constitute noise. Its application on a fully polarized SAR image acquired by the RadarSat-2 sensor over the city of Algiers showed its robustness and performance in identifying dominant scattering mechanisms according to their original class.

Acknowledgment

The authors would like to thank the Canadian Space Agency for supplying, as part of the SOAR program under the #1670 project, the polarimetric RADARSAT2 data used in this paper.

References

[1] A. Moreira, P. Prats-Iraola, M. Younis, G. Krieger, I. Hajnsek, and K. P. Papathanassiou, "A tutorial on synthetic aperture radar," *IEEE Geosci. Remote Sens. Mag.*, vol. 1, no. 1, pp. 6–43, Mar. 2013.

[2] S. M. Majd, "High-resolution polarimetric SAR image classification on urban areas," Ph.D. dissertation, Conservatoire nat. des arts et mtiers, Paris, France, 2014.

[3] J.-S. Lee and E. Pottier, *Polarimetric Radar Imaging: From Basics to Applications*. Boca Raton, FL, USA: CRC Press, 2009.

[4] S. Cloude, *Polarisation: Applications in Remote Sensing*. London, U.K.: Oxford Univ. Press, 2014.

[5] S.-W. Chen, Y.-Z. Li, X.-S. Wang, S.-P. Xiao, and M. Sato, "Modeling and interpretation of scattering mechanisms in polarimetric synthetic aperture radar: Advances and perspectives," *IEEE Signal Process. Mag.*, vol. 31, no. 4, pp. 79–89, Jul. 2014.

[6] X. Cheng, W. Huang, and J. Gong, "An unsupervised scattering mechanism classification method for PolSAR images," *IEEE Geosci. Remote Sens. Lett.*, vol. 11, no. 10, pp. 1677–1681, Oct. 2014.

[7] Y. Yamaguchi, *Polarimetric SAR Imaging: Theory and Applications* (ser. SAR Remote Sensing). Boca Raton, FL, USA: CRC Press, 2020.

[8] K. Karachristos, G. Koukiou, and V. Anastassopoulos, "A review on PolSAR decompositions for feature extraction," *J. Imag.*, vol. 10, no. 4, 2024, Art. no. 75.

[9] S. R. Cloude and E. Pottier, "An entropy based classification scheme for land applications of polarimetric SAR," *IEEE Trans. Geosci. Remote Sens.*, vol. 35, no. 1, pp. 68–78, Jan. 1997.

[10] S. R. Cloude, "Uniqueness of target decomposition theorems in radar polarimetry," in *Direct and Inverse Methods in Radar Polarimetry*. Berlin, Germany: Springer, 1992, pp. 267–296.

[11] S. R. Cloude and E. Pottier, "A review of target decomposition theorems in radar polarimetry," *IEEE Trans. Geosci. Remote Sens.*, vol. 34, no. 2, pp. 498–518, Mar. 1996.

[12] W. M. Boerner, W. L. Yan, A. Q. Xi, and Y. Yamaguchi, "Basic concepts of radar polarimetry," *Direct Inverse Methods in Radar Polarimetry*, NATO ASI Series, vol. 350, Springer, Dordrecht, 1992. [Online]. Available: https://doi.org/10.1007/978-94-010-9243-2_8

[13] W. A. Holm and R. M. Barnes, "On radar polarization mixed target state," in *Proc. USA Nat. Radar Conf.*, 1988, pp. 249–254.

[14] J. Yang, Y. N. Peng, Y. Yamaguchi, and H. Yamada, "On Huynen's decomposition of a Kennaugh matrix," *IEEE Geosci. Remote Sens. Lett.*, vol. 3, no. 3, pp. 369–372, Jul. 2006.

[15] S. R. Cloude, "Radar target decomposition theorems," *Electron. Lett.*, vol. 21, no. 1, pp. 22–24, 1985.

[16] J. Huynen, "Phenomenological theory of radar targets," Ph.D. dissertation, Dept. Elect. Eng., Math. Comput. Sci, Delft Univ. Technol., Delft, The Netherlands, 1970.

[17] R. Barnes, "Roll-invariant decompositions for the polarization covariance matrix," in *Proc. Polarimetry Technol. Workshop*, Redstone Arsenal, AL, USA, Aug. 16-18, 1988.

[18] R. Touzi, W. Boerner, J. Lee, and E. Lueneburg, "A review of polarimetry in the context of synthetic aperture radar: Concepts and information extraction," *Can. J. Remote Sens.*, vol. 30, no. 3, pp. 380–407, 2004.

[19] I. Hajnsek and Y.-L. Desnos, *Polarimetric Synthetic Aperture Radar: Principles and Application*, vol. 25. Berlin, Germany: Springer, 2021.

[20] D. M. Pozar, *Microwave Engineering*, vol. 148, 4th ed. Hoboken, NJ, USA: Wiley, 2011.

[21] A. Aubry, V. Carotenuto, A. De Maio, and L. Pallotta, "Assessing reciprocity in polarimetric SAR data," *IEEE Geosci. Remote Sens. Lett.*, vol. 17, no. 1, pp. 87–91, Jan. 2020.

[22] L. Pallotta, "Reciprocity evaluation in heterogeneous polarimetric SAR images," *IEEE Geosci. Remote Sens. Lett.*, vol. 19, 2020, Art. no. 4000705.

[23] D. G. Corr et al., "A review of the applications of SAR polarimetry and polarimetric interferometry—An ESA funded study," in *Proc. Workshop POLinSAR—Appl. SAR Polarimetry Polarimetric Interferometry*, 2003, pp. 1–9.

[24] E. Pottier, J.-S. Lee, and L. Ferro-Famil, "Advanced concepts in polarimetry—Part 1," Naval Research Lab., Washington, DC, USA, Tech. Rep. RTO-EN-SET-081, Oct. 2004, pp. 21–22.

[25] L. Pallotta and D. Orlando, "Polarimetric covariance eigenvalues classification in SAR images," *IEEE Geosci. Remote Sens. Lett.*, vol. 16, no. 5, pp. 746–750, May 2019.

[26] P. Addabbo, F. Biondi, C. Clemente, D. Orlando, and L. Pallotta, "Classification of covariance matrix eigenvalues in polarimetric SAR for environmental monitoring applications," *IEEE Aerosp. Electron. Syst. Mag.*, vol. 34, no. 6, pp. 28–43, Jun. 2019.

[27] F. Biondi, C. Clemente, and D. Orlando, "An eigenvalue-based approach for structure classification in polarimetric SAR images," *IEEE Geosci. Remote Sens. Lett.*, vol. 17, no. 6, pp. 1003–1007, Jun. 2020.

[28] P. Stoica and Y. Selen, "Model-order selection: A review of information criterion rules," *IEEE Signal Process. Mag.*, vol. 21, no. 4, pp. 36–47, Jul. 2004.

[29] C.-A. Deledalle, F. Tupin, and L. Denis, "Polarimetric SAR estimation based on non-local means," in *Proc. IEEE Int. Geosci. Remote Sens. Symp.*, 2010, pp. 2515–2518.

[30] K. Hadj-Rabah, G. Schirinzi, A. Budillon, F. Hocine, and A. Belhadj-Aissa, "Non-parametric tomographic SAR reconstruction via improved regularized music," *Remote Sens.*, vol. 15, no. 6, 2023, Art. no. 1599.

[31] I. T. Jolliffe, *Principal Component Analysis*, 2nd ed. New York, NY, USA: Springer, 2002.

Dehbia Hanis received the Engineering degree in electronics from Military Polytechnic School, Algiers, Algeria, in 2012, and the Master of Science degree in cartography and geographical information engineering from the State Key Laboratory of Information Engineering in Surveying, Mapping and Remote Sensing, Wuhan University, Wuhan, China, in 2017. She is currently working toward the Ph.D. degree in cartography and digital imaging with the Laboratory of Image Processing and Radiation, University of Science and Technology Houari Boumediene, Bab Ezzouar, Algeria, under the supervision of Prof. Aichouche Belhadj-Aissa.

In 2023, she was a Visiting Ph.D. Student with the Polytechnic University of Catalonia, Barcelona, Spain.

Karima Hadj-Rabah (Member, IEEE) received the M.Sc. degree in telecommunications, networks, and multimedia and the Ph.D. degree in radar remote sensing from the University of Sciences and Technology Houari Boumediene, Bab Ezzouar, Algeria, in 2016 and 2023, respectively.

In 2019, she was a Visiting Ph.D. Student with the Telecommunication Group, University of Naples "Parthenope," Napoli, Italy. Her research interests include synthetic aperture radar (SAR) applications with a focus on interferometry SAR and tomographic reconstruction SAR.

Aichouche Belhadj-Aissa received the Engineering degree in electronics from the National Polytechnic School, Algiers, Algeria, in 1980, and the Magister degree in image processing and the Doctorate degree in image processing and remote sensing from the University of Science and Technology Houari Boumediene (USTHB), Bab Ezzouar, Algeria, in 1985 and 1998, respectively.

She is a currently a Professor in Electronics, Image Processing, Remote Sensing and Geographic Information Systems and the Head of a Research Team with Electrical Engineering Faculty, USTHB. Her main research interests include modeling and analysis of textures and forms, fusion and classification of objects, synthetic aperture radar interferometry polarimetry, and its applications in detection and cartography of altimetric information and its variations.

Luca Pallotta (Senior Member, IEEE) received the Laurea Specialistica (*cum laude*) degree in telecommunication engineering from the University of Sannio, Benevento, Italy, in 2009, and the Ph.D. degree in electronic and telecommunication engineering from the University of Naples Federico II, Naples, Italy, in 2014.

From 2019 to 2022, he was an Assistant Professor with the University of Roma Tre, Rome, Italy. He is currently an Assistant Professor with the University of Basilicata, Potenza, Italy. His research interests include statistical signal processing, with emphasis on radar/synthetic aperture radar (SAR) signal processing, radar target detection and classification, and polarimetric radar/SAR.

Dr. Pallotta won the Student Paper Competition at 2013 IEEE Radar Conference. Since 2020, he has been an Associate Editor for IEEE JOURNAL OF SELECTED TOPICS IN APPLIED EARTH OBSERVATIONS AND REMOTE SENSING. From 2018 to 2021, he was an Associate Editor for *Signal, Image and Video Processing*.

Open Access funding provided by 'Università degli Studi della Basilicata' within the CRUI CARE Agreement